Journal of Applied Polymer Science

Effective permittivity of nanocomposites from 3D charge transport simulations

Meng H. Lean, Wei-Ping L. Chu
QEDone LLC, 4174 Marston Lane, Santa Clara California 95054
Correspondence to: M. H. Lean (E-mail: mhlean@ieee.org)

ABSTRACT: The effective permittivity and stored energy in nanocomposites incorporating dielectric and conducting nanofillers are computed by simulating bipolar charge injection, transport, attachment, and recombination through amorphous polymer using a self-consistent 3D particle-in-cell model with nanofillers treated as extensions to the classical electrical double layer. Effective permittivities computed using an energy conserving scheme is shown to have excellent agreement with the Lichtenecker, Bruggeman, and Maxwell-Garnett mixing rules especially at low volume fraction, low permittivity contrast, and small Clausius-Mossotti factor, and lie well within the Wiener bounds. The energy conserving scheme with Maxwell-Garnett **E** field interpolation combines the best of the Maxwell-Garnett and fundamental Lichtenecker rules and results in broad validity over the entire volume fraction range. Computed stored energies show monotonic increase with dielectric fillers and a peak at 25 vol % for conducting fillers, attributed to the competing effects of higher energy with increasing **E** field modification and lower energy with decreasing binder volume. © 2015 Wiley Periodicals, Inc. J. Appl. Polym. Sci. **2016**, *133*, 43300.

KEYWORDS: amorphous; composites; nanoparticles; nanowires and nanocrystals; nanostructured polymers; theory and modeling

Received 25 September 2015; accepted 1 December 2015
DOI: 10.1002/app.43300

INTRODUCTION

Nanocomposite films incorporating well-dispersed ceramic nanofillers within amorphous polymer binders are used as inexpensive, lightweight, self-healing capacitors for energy storage in rapid power cycling applications.[1] High permittivity ceramic nanofillers (with typically low breakdown strength) are combined with high breakdown strength polymers (with typically low permittivity) in the right proportion, size range, and/or polarization to result in nanocomposite films with high energy density, U_e, given by $U_e = \int EdD$, where E is the applied electric field and D is the electric displacement. The effective permittivity of the nanocomposite is typically calculated using one of the well-known Lichtenecker, Bruggeman, or Maxwell-Garnett mixing rules; derived assuming purely Laplacian fields. It is an accepted fact that the validity of these rules are limited to low filler loading of less than 10-15 vol %.[2] High contrast in permittivity between the diphasic composite give rise to highly inhomogeneous electric fields (**E**) in the "interaction zone", defined as the interfacial region that surrounds the nanofillers and interspaces. These **E** fields together with structural inhomogeneity generally lead to a significant reduction in the effective breakdown field strength of the composite, limiting the increase in the energy storage capacity and energy density, and directly impacting the effective permittivity. The challenge in matching nanofillers with the polymer matrix is to understand the role of the interaction zone where the very large area to volume ratio of the interfaces in nanocomposites has significant impact on the electrical and dielectric properties of the film.

Charge mapping studies help to define and quantify the taxonomy of the mobile, trapped, bound, and polarization charge types and their abundance. Knowledge of the spatial and temporal charge distributions facilitate insight into the dynamics of charge redistributions which lead to breakdown at high fields or prolonged usage. Empirical methods using pulse electroacoustic (PEA) and laser induced pressure pulse (LIPP) techniques have demonstrated preliminary feasibility.[3,4] 1D bipolar charge transport models have described LDPE results.[5,6] Recently, a hybrid algorithm capable of handling leakage current up to prebreakdown levels have been successfully applied to layered polymer films and simulated PEA measurements.[7] Axisymmetric models capable of handling divergent field configurations have also been reported.[8,9] However, continuum charge transport models are not suited to simulate material with morphology at the nanometer length scale. Several models of nanoparticles are discussed in the literature, including the Tanaka Multicore 3-layer and the Lewis models.[10] The classical electrical double layer (EDL) is similar to the Lewis model and is predicated on a monopole net charge for the core. Charge transport is enabled

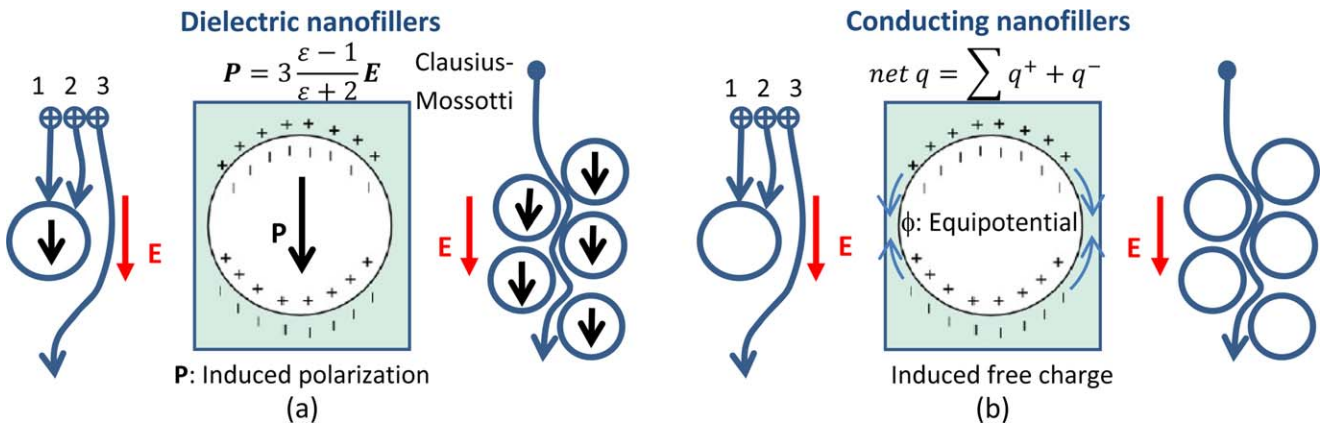

Figure 1. (a) Extended EDL model for dielectric nanofiller (e.g., Al_2O_3) in amorphous polymer (e.g., PA/PAI) binder where initial charge "1" attach to upper hemisphere of nanofiller followed by "2" until Coulomb repulsion from charge build-up allow subsequent particle "3" to pass resulting in MWS polarization effect; and (b) EDL model for conducting nanofillers in amorphous polymer where impacted bipolar charge migrate freely on the surfaces and recombine, resulting in equipotentials and Coulomb repulsion from net charge leading to particle trajectories meandering through the interspaces. [Color figure can be viewed in the online issue, which is available at wileyonlinelibrary.com.]

by the increase in nanoparticle loading within the dielectric composite eventually leading to overlap of the diffuse double layers forming conduction paths. Bulk charge accumulation is reduced due to this internal conductivity, and the dielectric breakdown strength of the nanocomposite is improved.

This paper simulates the use of dielectric Alumina (Al_2O_3) and conducting nanofillers in a polyamide/polyimide (PA/PAI) binder using a self-consistent particle simulation model. The EDL model is extended by substitution of a dipolar core and used for dielectric nanofillers as shown in Figure 1(a) where the induced polarization aligns with the bias electric field. The classical EDL model is used for conducting nanofillers as shown in Figure 1(b). Charge passage with dielectric nanofillers may be illustrated in Figure 1(a), where incoming positive charge is repelled by the positive-end and attracted towards the negative-end of the dipole and vice-versa. Charge is allowed to attach on impact forming the bound Stern-Helmholtz layer. Subsequent waves of incoming charge are repelled to form the diffuse outer Gouy-Chapman transport layer. The cumulative charge buildup on opposing ends of the dipole leads to Maxwell-Wagner-Sillars (MWS) polarization. The gradual charge deposition and formation of the diffuse layers as charge migrates through the polymer film creates the interaction zone. Trajectories for charges that make it through the film to the counter-electrode are curvilinear paths that meander through the interspaces. The corresponding description for conducting nanofillers is shown in Figure 1(b). For bipolar charge, the initial charge "1" impacts the upper hemisphere of nanofiller followed by "2" subject to recombination and net charge repulsion. In the unipolar case, Coulomb repulsion from net charge may repel subsequent particle "3". Induced free charge and impacted charge create an equipotential surface on the nanofiller. Charges that arrive at the counter-electrode are neutralized and therefore contribute to the conduction of the film; but not to the field. Metal-polymer charge injection assumes Schottky emission and Fowler-Nordheim tunneling, migration through field-dependent Poole-Frenkel mobility, and recombination with Monte Carlo selection. A boundary integral equation method (BIEM) is used for solution of the Poisson equation coupled with a second-order predictor-corrector scheme for robust time integration of the equations of motion. The stability criterion of the explicit algorithm conforms to the Courant-Friedrichs-Levy (CFL) limit. This paper will discuss an energy conserving scheme to compute effective permittivity and stored energy in nanocomposites and compare results for dielectric or conducting fillers. The calculation will be based on results from bipolar charge injection, transport, and recombination (electroluminescence) through nanocomposite film comprising dielectric Alumina and conducting nanofillers in amorphous polyamide/polyimide binder for a range of nanofiller vol % loading.

MIXING RULES

The effective permittivities of nanocomposites may be calculated from several well-known mixing rules. The Lichtenecker rule is traditionally derived from Wiener theory for the effective permittivity, ε_L, of two-phase anisotropic composites given by[11]:

$$\varepsilon_L^k = \phi_f \varepsilon_f^k + \left(1 - \phi_f\right)\varepsilon_b^k \tag{1}$$

where ϕ_f is the volume fraction of inorganic filler and ε_f and ε_b are, respectively, the permittivities of the filler and polymer binder. From Wiener theory, $k = 1$ determines the upper bound for plane-parallel layers and $k = -1$ sets the lower bound for layers perpendicular to the applied field with physical implications of capacitances in parallel and in series. The logarithmic rule results from a special case of the power law model in the limit as $k \to 0$, resulting in[12]:

$$ln\,\varepsilon_L = \phi_f \ln\ \varepsilon_f + \left(1 - \phi_f\right) ln\,\varepsilon_b \tag{2}$$

Macroscopic semi-analytic mixing notions based on the mean field theory (MFT) have been applied to predict the effective dielectric properties of mixtures without having to deal with the details of microscopic fields. The effective medium approximation (EMA) approach replaces the physical diphasic problem of multiple inclusions in an inhomogeneous medium with a single

inclusion surrounded by an effective homogeneous medium with permittivity determined self-consistently. The symmetric Bruggeman model for a spherical inclusion in a homogeneous polymer binder is given by[13]:

$$\phi_f\left(\frac{\varepsilon_f-\varepsilon_B}{\varepsilon_f+2\varepsilon_B}\right)+\left(1-\phi_f\right)\left(\frac{\varepsilon_b-\varepsilon_B}{\varepsilon_b+2\varepsilon_B}\right)=0 \quad (3)$$

where ε_B is the Bruggeman effective permittivity, and both terms carry the respective Clausius-Mossotti factors. These expressions represent the strengths of the polarization fields for small electrically homogeneous spherical inclusions of permittivities, ε_f and ε_b, embedded in a homogeneous medium of effective permittivity, ε_B. This equation is derived using the uniform electric field inside the spherical filler and imposing the self-consistent condition required by the EMA whereby the average field inside the filler should equal the average field in the homogeneous medium.

Derivation of the Maxwell-Garnett formula from the MFT requires consideration of an array of polarizable and separated particles, use of the Clausius-Mossotti factor, and incorporating the polarization influence of neighboring particles to obtain[14]:

$$\left(\frac{\varepsilon_{MG}-\varepsilon_b}{\varepsilon_{MG}+2\varepsilon_b}\right)=\phi_f\left(\frac{\varepsilon_f-\varepsilon_b}{\varepsilon_f+2\varepsilon_b}\right) \quad (4)$$

An integral average may also be obtained by sampling the permittivity, summing over the filler and binder volumes, V_f and V_b, and then dividing out by the volume, V, of the composite:

$$\varepsilon_{vf}=\frac{\int_V \varepsilon_i dV}{\int_V dV}=\frac{\int_{V_f} \varepsilon_f dV_f+\int_{V_b} \varepsilon_b dV_b}{\int_V dV}=\phi_f\varepsilon_f+\left(1-\phi_f\right)\varepsilon_b \quad (5)$$

where

$$\varepsilon_i=\begin{cases}\varepsilon_f; & r_i \in filler\\ \varepsilon_b; & r_i \in binder\end{cases} \quad (6)$$

which results in the volume fraction approximation of linearly interpolated permittivity, identical to the upper bound of the Lichtenecker rule with $k=1$ in (1).

Generally, the Bruggeman and Maxwell-Garnett formulae are valid at low volume fractions due to the assumption that the spherical inclusions are spatially separated. Beyond the infinite wavelength or quasi-static limit, the EMA can also be generalized to finite frequencies, provided the size of the inhomogeneity is small relative to the wavelength of the electric field in the composite medium. An implicit assumption is that the electric fields and displacements should be approximately uniform within any given inclusion of the inhomogeneous medium.

A rigorous derivation of the Lichtenecker rule starting from Maxwell's equations and invoking charge conservation between the heterogeneous mixture and the homogeneous effective medium representation was recently reported.[15] A key assumption is to replace the charge density at any position by the mean charge density of the mixture thereby allowing the charge fraction to be replaced by the volume fraction. The Lichtenecker rule was derived for random distributions without any restriction on the shapes of the inclusions. Using the Clausius-Mossotti factor, $(\varepsilon_f-\varepsilon_b)/(\varepsilon_f+2\varepsilon_b)$, which defines the magnitude of the polarization field for an electrically small dielectric spherical inclusion of permittivity, ε_f, embedded in a homogeneous medium of permittivity, ε_b, and taking only the first (linear) term of the binomial expansion results in the Maxwell-Garnett formula. Thus the Maxwell-Garnett is shown to be an approximation to the Lichtenecker rule for small volume fractions, spherical inclusions, and small Clausius-Mossotti factor. Similarly, the symmetric Bruggeman rule is derived from the Lichtenecker rule by treating the two Clausius-Mossotti factors: $(\varepsilon_f-\varepsilon_B)/(\varepsilon_f+2\varepsilon_B)$ and $(\varepsilon_b-\varepsilon_B)/(\varepsilon_b+2\varepsilon_B)$ in the same manner, i.e. assuming spherical inclusions, only first order interactions between inclusions, small permittivity contrast, and small Clausius-Mossotti factors. The simplifying assumptions to derive the Maxwell-Garnett and Bruggeman rules from the Lichtenecker rule suggest that the Lichtenecker rule is more fundamental in nature.

Commercial software has been used to compute the complex effective permittivity of nanocomposites using the Drude free electron model and a bound electron term.[16] Other methods of frequency dependent calculation include the use of impedance cells,[17] and equivalence capacitance model,[18] and solution of the Maxwell equations for wave propagation using finite-difference time-domain (FDTD) in 2D[12] where the authors claim that no model seems able to predict the simulated behavior over the entire range of volume fractions.

CHARGE TRANSPORT ALGORITHM

Formulation of the bipolar charge transport algorithm involves particle simulation of ensemble charge motion in an electrostatic field implemented as a time-iterative two-step approach of field-solve and particle-push. The equations of motion are integrated within a computational cell subject to periodic boundary conditions and particle interactions with random distributions of nanofillers in an amorphous polymer binder. This self-consistent model includes consideration for charge injection, transport, attachment/detachment, and recombination. Only salient features of this algorithm are briefly discussed here as it is not the focus of this paper. Complete details are available in the literature.[19–22]

Field Solution and Particle Simulation

The computational cell used for the nanoscale simulations is shown in Figure 2 where the 500 nm nanocomposite layer is sandwiched between two 250 nm amorphous polymer layers. The cell is a cuboid of edge dimension 1 μm, volume of 1 μm^3, bounded by 4 vertical side walls with zero flux condition ($\partial\phi/\partial n = 0$), and top (anode) and bottom (cathode) electrodes at constant potential to maintain the bias **E** field. Periodic boundary conditions imposed on the 4 vertical walls force exiting particles to re-enter at the opposite side walls. The composite **E** field has contributions from the bias voltage, injected mobile charge, attached charge on nanofillers, and free charge on conducting fillers or polarization field from dielectric fillers. The solution of the Poisson equation is obtained using the boundary integral equation method (BIEM), based on the use of the free space Green function as the solution to a point source. Instead of the classical approach of deriving a particular Green function

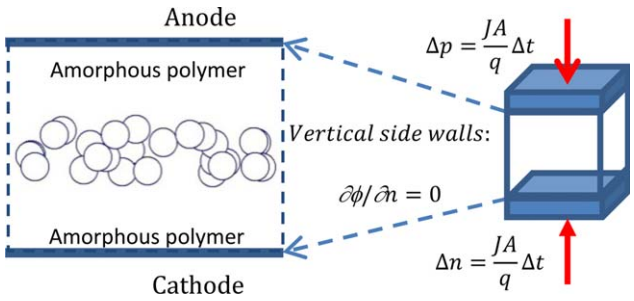

Figure 2. Side view of computational cell with 500 nm nanocomposite layer sandwiched between 250 nm layers of amorphous polymer, current injection through upper and lower electrodes, and zero flux boundary conditions for vertical walls. [Color figure can be viewed in the online issue, which is available at wileyonlinelibrary.com.]

that incorporates geometry, material properties, and boundary conditions, linearity and superposition is invoked to solve an equivalent (and simpler) problem. The source distribution technique (SDT) treats mobile space charge and bulk trapped charge as volume sources, and replaces conducting boundaries and material interfaces with appropriate distributions of unknown free and bound interfacial polarization and trapped charges to satisfy the specified boundary and interface conditions. Enforcement of boundary conditions for potential and flux and interface conditions at material interfaces for continuity of tangential **E** and normal **D** ($=\varepsilon\mathbf{E}$) for Dirichlet, Neumann, and dielectric interface conditions, respectively, result in a system of integral equations for the unknown charge densities. For conducting nanofillers, bipolar mobile charge that impact are treated as free charge that migrate on the surface and therefore neutralize, resulting in a net charge which together with the charge induced by the bias field create a floating equipotential. Since this potential is not known *apriori*, an additional equation is required for each nanofiller to augment the system of equations in order to solve for these equipotentials.

Selective enforcement at collocation points discretized the equations resulting in a matrix that is inverted to determine the magnitude of the free and bound polarization source distributions. Then fields and field derivatives are then computed by integrating contributions from all the source distributions. Kernel functions, including the Green function and its analytic derivatives (G, ∂G/∂n, and ∇G) are integrated numerically using Gauss-Legendre quadrature. Singular kernels are accurately computed using minimum order sampling by tying the quadrature weight function to the singularity. Details on the computation of these integrals are discussed in detail for axisymmetric and 2D geometries.[7–9] Discretized forms of these equations are solved simultaneously for free charge on electrodes and bound charge on material and physical interfaces to fully determine the Poisson solution.

Nanofillers are randomly distributed within the cell to the prescribed vol % loading using "hard sphere" logic; i.e., allowing contact but no over-lap. Discrete numbers of charge particles, dictated by the current density and time-step, are continuously injected from the electrodes as a function of the averaged electrode **E** field. Injection locations are randomly dispersed over the electrode surface. Charge particles migrate through the nanofiller distribution under the composite **E** field subject to particle-particle interactions, and particle attachment to nanofillers with those arriving at the counter-electrode considered neutralized and therefore having no further contribution to the **E** field. Particle tracking involves a predictor-corrector algorithm of order Δt^2, or second-order accurate in time, to integrate the equations of motion subject to the applied bias. To minimize local error, displacement, Δh, is required to be smaller than the Debye length, i.e. $L_D = (\varepsilon k_B T/q^2 N_i)^{1/2}$, where N_i is the largest charge number density. The time step, Δt, needs to be shorter than the dielectric relaxation time, $\tau = \varepsilon/qN_i\mu$, characteristic of charge fluctuations to decay. The stability criterion of the explicit algorithm is given by the CFL limit, $c=|v\Delta t/\Delta h| \leq 1$, which represents the ratio of mobile charge velocity, v, to trace velocity, $\Delta h/\Delta t$. For stability, the trace velocity cannot be faster than the speed of the charge.[23] A tacit assumption is that the field is "frozen-in" relative to the time step of charge migration, and the transient time to attain terminal velocity is much shorter than the mean free path or the time between collision events of oppositely charged particles. A self-consistent particle-particle, particle-mesh (P^3M) scheme may be implemented for very large numbers of particles.[24–26]

Charge Injection, Transport, Attachment, and Recombination

At low to moderate applied fields, charge injection from a metal electrode into the lowest unoccupied molecular orbital (LUMO) band of the polymer is by Schottky barrier thermionic emission where the combined effect of the image force and the applied field result in a lowering of the barrier potential. At higher applied fields, the slope is steeper and the barrier is further lowered so that the tunneling length is much shorter, increasing the probability for tunneling through the barrier. Charge injection from a metal electrode into the polymer is treated using the Fowler-Nordheim quantum mechanical tunneling model.

At low-fields and low densities, carriers are almost in equilibrium with the lattice vibrations so low-field mobility is mainly affected by phonon and Coulomb scattering. The mobility increases until the velocity approaches the random thermal velocity. In a moderately large electric field, less thermal fluctuation is required to free charge allowing for higher conduction via the Poole-Frenkel mobility. At higher electric fields, mobility decreases with increasing electric field due to increased lattice scattering at higher carrier energies, and carrier velocity saturate. The Caughey-Thomas field-dependent mobility is used to provide a smooth transition between low-field and high field behavior.[27]

Trapped charge on nanofiller surfaces are considered to be attached charge. In the EDL model, initial charge attachment to nanofillers are assumed to be deterministic, i.e. attachment on impact, or probability $P_t(t)=1$. Subsequent taper-off due to Coulomb force and dipole field repulsion from build-up of the attached charge follow the MWS effect, i.e., $P_t(t)\rightarrow 0$ as the limiting behavior. Charge detachment may be physically controlled by comparing the local field to the trap depth in the de-trapping rate.[7]

The Monte Carlo collision model is used to describe particle-particle events between oppositely charged entities resulting in recombination.[25] The probability of a collision of the i^{th} charge particle with a charge particle of the opposite polarity in a time step Δt is $P_i = 1 - e^{-n_0 \sigma(E_i) v_i \Delta t}$, where n_0 is the number density of the opposite polarity mobile charge, $\sigma(E_i)$ is the total collision cross-section which in general depends on the kinetic energy of the i^{th} particle (could be larger than the geometrical cross-section, $\sigma = \pi\left(r_i + r_j\right)^2$), and v_i is the velocity of this particle relative to the velocity of the opposite polarity particle. Therefore, $n_o\sigma$ is a measure of the number of collisions per unit length, $1/n_o\sigma$ is the mean free path between collisions, and $n_o\sigma v_i$ is the collision frequency. For a finite Δt, the probability of a collision is determined by comparing P_i with R_i, a uniform random number between 0 and 1. For $P_i > R_i$, particle i is considered to have sustained a collision within the time step Δt resulting in recombination and neutralization of the charge pair. Otherwise, Monte Carlo selection returns a nonevent.

ENERGY CONSERVING SCHEME

The 3D PIC model is used for dynamical solution of the charge transport equations to compute stored energy and derive effective DC permittivity through an energy conserving scheme without any restrictions on particle interactions, permittivity contrast, or magnitude of the Clausius-Mossotti factors. The steps to this scheme are as follows:

1. Map 1D Gauss-Jacobi quadrature into 3D orthogonal distribution to integrate the computational cell as a single volume entity where the numerical quadrature to integrate $F(x) = w(x)f(x)$ is expressed as the summation of the sampled function with the corresponding weight:

$$\int_a^b F(x)dx = \sum_{i=1}^{\infty} w_i f(x_i) \approx \sum_{i=1}^{n} w_i f(x_i) \tag{7}$$

The Gauss-Jacobi quadrature is a specialized form given by[28]:

$$\int_{-1}^{+1} (1-x)^{\alpha}(1+x)^{\beta} f(x)dx = \sum_{i=1}^{n} A_i f(x_i) + 0(h)^n \tag{8}$$

Using $\alpha = 0$, $\beta = 0$, simplifies the integrand to $f(x)$. Sampling locations, x_i, are the n roots of the Gauss-Jacobi polynomial, $P_n^{(\alpha,\beta)}(x)$, of degree n, and A_i are the coefficients of x_i in $P_n^{(\alpha,\beta)}(x)$ given by:

$$A_i = -\frac{2n+\alpha+\beta+2}{n+a+b+1}\frac{\Gamma(n+a+1)\Gamma(n+b+1)}{(n+a+b+1)(n+1)!}\frac{2^{\alpha+\beta}}{P_n'(x_i)P_{n+1}'(x_i)} \tag{9}$$

2. Assume permittivity, ε_i, or field, E_i, as 3D distributions defined by the random distributions of filler in the binder within the computational cell and sample according to (6) and:

$$E_i = \begin{cases} E_f; & r_i \in filler \\ E_b; & r_i \in binder \end{cases} \tag{10}$$

where ε_i and E_i take on filler or binder values based on the sampling location.

3. Compute energy, W, using:

$$W = \int_V \frac{1}{2}\varepsilon_0\varepsilon_r E^2 dV \approx \sum_{i=1}^{m} \frac{1}{2}\varepsilon_0\varepsilon_i E_i^2 = \sum_{i=1}^{m} \frac{1}{2}\varepsilon_0\varepsilon_{eff} E_{ave}^2 \tag{11}$$

where E_{ave} for dielectric and conducting fillers are, respectively, given by:

$$E_{ave} = \frac{\int_V E_i dV}{\int_V dV} = \frac{\int_{V_f} E_f dV_f + \int_{V_b} E_b dV_b}{\int_V dV} \approx \langle E_f\rangle\phi_f + \langle E_b\rangle\left(1-\phi_f\right) \tag{12}$$

and

$$E_{ave} = \frac{\int_V E_i dV}{\int_V dV} = \frac{\int_{V_b} E_b dV_b}{\int_{V_b} dV_b} \approx \langle E_b\rangle\left(1-\phi_f\right) \tag{13}$$

with the field, E_f, vanishing in the interior of the conducting filler and angular brackets denoting volume average. In (12), the volume averaging reduces to a volume fraction (linear) interpolation of the **E** field between the volume averaged fields in the filler and the binder.

4. Equating energy expressions in (11) and substituting for the average electric field, E_{ave}, results in an expression for the effective permittivity, ε_{eff}:

$$\varepsilon_{eff} = \frac{\int_V \varepsilon_i E_i^2 dV}{E_{ave}^2 \int_V dV} = \frac{\langle W'\rangle}{E_{ave}^2} = \frac{\langle W'\rangle}{\left[\langle E_f\rangle\phi_f + \langle E_b\rangle\left(1-\phi_f\right)\right]^2} \tag{14}$$

with the volume averaged energy-related parameter, $\langle W'\rangle$, given by:

$$\langle W'\rangle = \frac{\int_V \varepsilon_i E_i^2 dV}{\int_V dV} \tag{15}$$

An intuitive alternative for **E** field interpolation is the Maxwell-Garnett formula with ε replaced by E:

$$E_{MG} = E_b + 3\phi_f E_b \frac{E_f - E_b}{E_f + 2E_b - \phi_f\left(E_f - E_b\right)} \tag{16}$$

The asymptotic limits for effective permittivities are given by:

$$\begin{aligned} \lim_{\phi f \to 1}\varepsilon_{eff} &= \frac{\langle W'\rangle}{\left[\langle E_f\rangle + \phi_f + \langle E_b\rangle\left(1-\phi_f\right)\right]^2} \sim \frac{\langle W'\rangle}{\left[\langle E_f\rangle\right]^2} \\ \lim_{\phi f \to}\varepsilon_{eff} &= \frac{\langle W'\rangle}{\left[\langle E_f\rangle + \phi_f + \langle E_b\rangle\left(1-\phi_f\right)\right]^2} \sim \frac{\langle W'\rangle}{\left[\langle E_b\rangle\right]^2} \end{aligned} \tag{17}$$

where $\langle E_b\rangle \gg \langle E_f\rangle$. The rate of change of effective permittivity with volume fraction is given by:

$$\frac{d\varepsilon_{eff}}{d\phi_f} = \frac{2\langle W'\rangle\left(\langle E_b\rangle - \langle E_f\rangle\right)}{\left[\langle E_f\rangle\phi_f + \langle E_b\rangle\left(1-\phi_f\right)\right]^3} \tag{18}$$

with the asymptotic limits:

$$\begin{aligned} \lim_{\phi_f \to 1}\frac{d\varepsilon_{eff}}{d_{\phi_f}} &= \frac{2\langle W'\rangle\left(\langle E_b\rangle - \langle E_f\rangle\right)}{\left[\langle E_f\rangle\right]^3} > 0 \\ \lim_{\phi_f \to 0}\frac{d\varepsilon_{eff}}{d_{\phi_f}} &= \frac{2\langle W'\rangle\left(\langle E_b\rangle - \langle E_f\rangle\right)}{\left[\langle E_b\rangle\right]^3} > 0 \end{aligned} \tag{19}$$

so that with $\langle E_b\rangle \gg \langle E_f\rangle$, the inference is:

Table I. Simulation Parameters

Parameter	Value	Description
μ_p	9×10^{-11} cm^2/V.s	Mobility of positive charge
μ_n	9×10^{-11} cm^2/V.s	Mobility of negative charge
W_p	1.2 eV	Anode barrier potential
W_n	1.2 eV	Cathode barrier potential
$\varepsilon_{PA/PAI}$	4.9	Dielectric constant PA/PAI
$\varepsilon_{Alumina}$	8.5.	Dielectric constant Alumina
$d_{Alumina}$	100 nm	Diameter of Alumina
vol %	1.0 – 66.0%	Nanofiller loading

$$\frac{d\varepsilon_{eff}}{d\phi_f}|_{\phi_f \to 1} \gg \frac{d\varepsilon_{eff}}{d\phi_f}|_{\phi_f \to 0} \tag{20}$$

Since E_{ave} decreases linearly with increasing ϕ_f, the effective permittivity increases as $1/E_{ave}^2$, and the gradient increases as $1/E_{ave}^3$, or at an increasingly higher rate.

RESULTS AND DISCUSSION

The model for the nanocomposite film is a random distribution of 100 nm spherical Alumina or conducting nanofillers between 1.0 to 66.0 vol % loading in a PA/PAI binder. The sample is a 500 nm layer sandwiched on the top and bottom by 250 nm amorphous polymer layers. Detailed results are generated about the triplet: $\boldsymbol{E} = 100$ V/μm, 100 nm nanofiller size, and 4.0 vol % to illustrate the capability of the 3D charge transport model. Effective permittivity and stored energy for dielectric and conducting nanofillers are computed over the loading range with run times adjusted to ensure the same amount of injected charge to compare results. Table I summarizes the simulation parameters used which are drawn from Refs. 5–7. For discussion, define the charge that arrives at the counter-electrodes as leakage conduction charge. Previous studies on ferroelectric $BaTiO_3$ (with similar field behavior to other Perovskites such as TiO_2, or ZrO_2) in PVDF have determined that anti-parallel polarization results in the highest leakage conduction and the lowest level of charge trapping in the interaction zone.[19–22]

Figures 3(a,b) show the perspective views of 3D scatter plots for randomly distributed 100 nm Alumina or conducting nanofillers (large blue circles) at 4.0 vol % loading, and positive and negative attached charge (red and blue dots), mobile charge (crimson and cyan dots), and leakage conduction charge at the counter-electrodes (rouge and navy dots) for dielectric and conducting nanofiller, respectively. Bipolar charge attachment to the nanofillers, i.e. positive to the upper hemisphere and negative to the lower hemisphere are clearly illustrated where in the case of Figure 3(b), opposite signed charge undergoes charge neutralization.

Charge arrived at the counter electrodes form uniquely distinct patterns resulting from the impact locations of the meandering conduction paths through the nanofiller distributions. Empty areas indicate more field deflection in the case of dielectric nanofillers. More solid area patterns generally indicate higher leakage conduction.

Electroluminescence (EL) in dielectric polymers is attributed to hot carrier impact ionization and/or bipolar charge recombination. Both processes point to the release of energy which dissipates through pathways leading to eventual chemical degradation.[29] Shown in Figure 4(a,b) are the top views of recombination scatter plots for dielectric and conducting nanofillers, respectively, where large blue circles are the nanofillers and red dots denote recombination sites of mobile charge pairs. Bipolar charge recombination is computed from collision probability and results in sites that are distributed only within the polymer binder. Recombination is more extensive for conducting nanofillers due to higher leakage conduction.

In Figure 5(a,b), the normal components of **E** fields averaged over the electrodes are plotted in time for the dielectric and conducting nanofillers. The initial dip in **E** field is due to accumulation of injected charge adjacent to the electrodes prior to migration away through the nanocomposite layer. Arrival of counter charge after 1 transit time reduces the space charge effect which allows the field to re-elevate. The slight difference (<1%) in vertical **E** field is due to the random depth distribution of nanofillers which is biased 1.14% towards the anode. Larger peaks and steady-state amplitudes are observed for the conducting nanofillers. Figure 6(a,b) show the injected positive current densities using Schottky emission for the dielectric and conducting nanofillers, respectively, where the initial dips follow the dips in the **E** field as seen in Figure 5(a,b). Injected positive

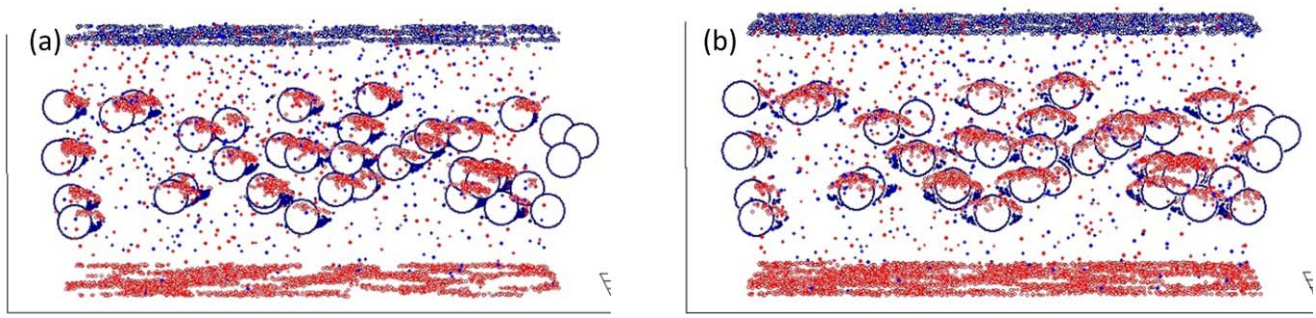

Figure 3. Side view scatter plots of randomly distributed nanofillers and mobile, conduction, and attached bipolar charge within the computational cell with uniquely different distributions of positive (rouge) and negative (navy) leakage conduction charge arrived at the counter-electrodes (lower cathode and upper anode) for: (a) dielectric nanofillers; and (b) conducting nanofillers. [Color figure can be viewed in the online issue, which is available at wileyonlinelibrary.com.]

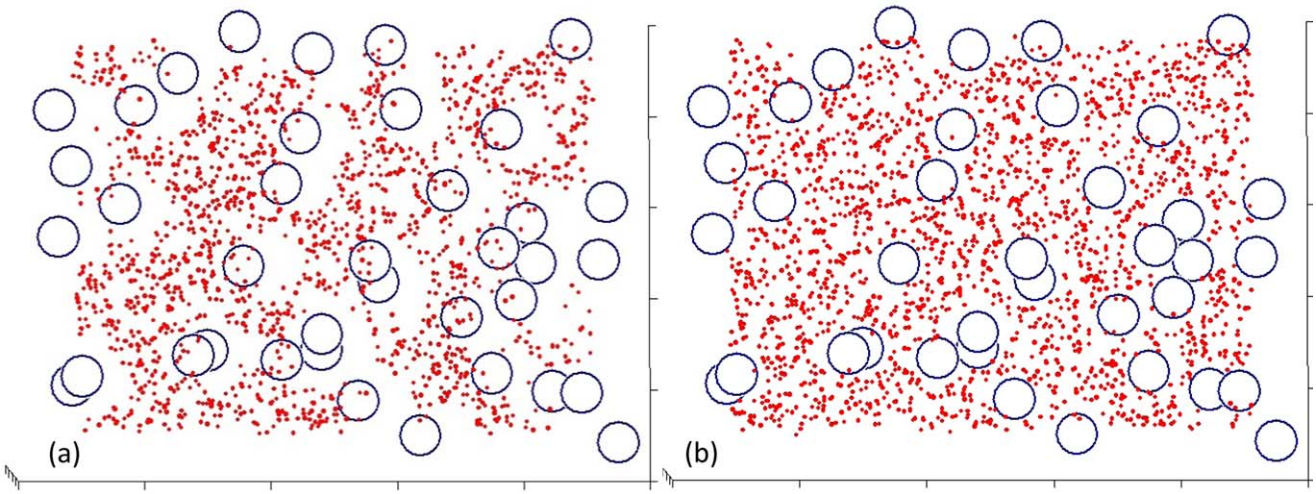

Figure 4. Top view scatter plots with nanofillers (blue circles) and recombination sites (red dots) which are clustered only in the open spaces in the polymer binder for: (a) dielectric; and (b) conducting nanofillers. [Color figure can be viewed in the online issue, which is available at wileyonlinelibrary.com.]

and negative currents are nearly identical so only the positive polarity is shown here. Shown in Figure 7(a,b) are the positive charge fractions for attached, conduction, mobile, and recombined components of the dielectric and conducting nanofillers, respectively. Positive and negative charge fractions are nearly identical so only the positive is shown here. The fractions asymptote with time to steady-state levels. There is a higher level of attached charge than conduction charge for dielectric nanofillers and vice versa for conducting nanofillers.

Figure 8(a,b) show leakage conductivity of the positive and negative mobile charge over time, calculated from current continuity as the ratios of charge density arriving on the surface to the surface-averaged **E** field on the counter electrodes:

$$\sigma_p = \frac{+q/\text{Area}}{E_{\text{cathode}}}\left(\frac{\Delta p}{\Delta t}\right)$$
$$\sigma_n = \frac{q/\text{Area}}{E_{\text{anode}}}\left(\frac{\Delta n}{\Delta t}\right) \quad (21)$$

where Δp and Δn are the number of charge particles that arrive in time Δt. Conductivities of cases with dielectric and conducting nanofillers are calculated using (21) for 100 nm particles at $\boldsymbol{E} = 100$ V/μm and 4.0 vol % loading, a level below the percolation threshold. The estimates stabilize after about 5 transit times, probably due to the dynamics in the interaction zone, to $\sim$0.32 x 10^{-14} S/cm for dielectric nanofillers, in agreement with published data for plastics of 0.3 x 10^{-14} S/cm. Higher leakage conductivities of 0.4 x 10^{-14} S/cm is seen for conducting

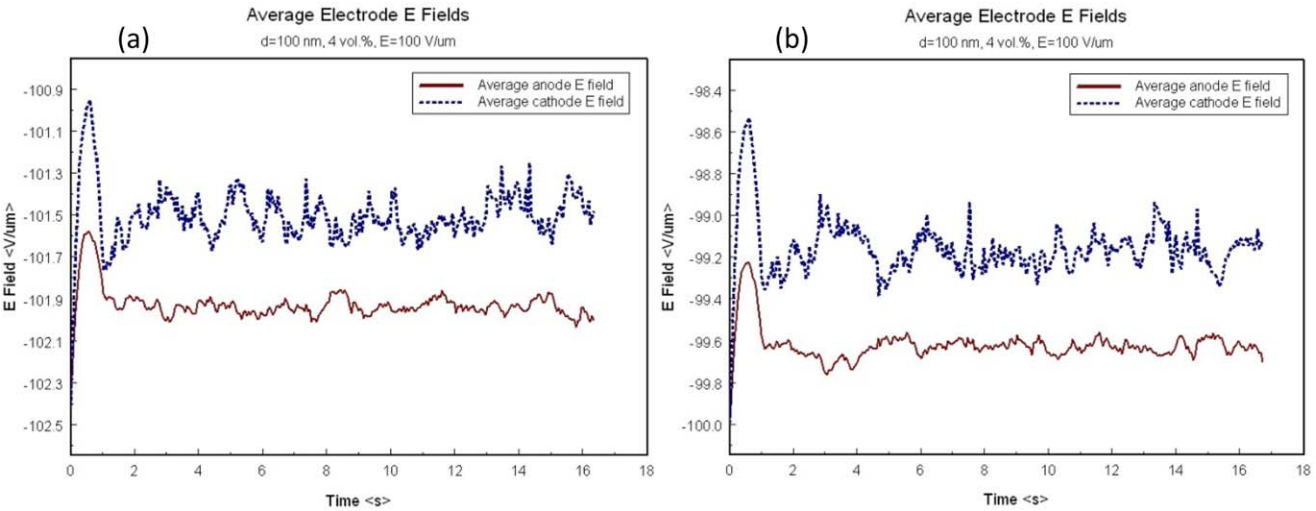

Figure 5. (a) Dielectric; and (b) conducting nanofiller **E** fields averaged over electrodes where initial dips are due to accumulation of injected charge adjacent to electrodes before migration through nanocomposite and subsequent arrival of counter charge after 1 transit time. The slight difference (<1%) in vertical **E** field is due to random depth distribution of nanofillers which is skewed towards the anode by 1.14%. [Color figure can be viewed in the online issue, which is available at wileyonlinelibrary.com.]

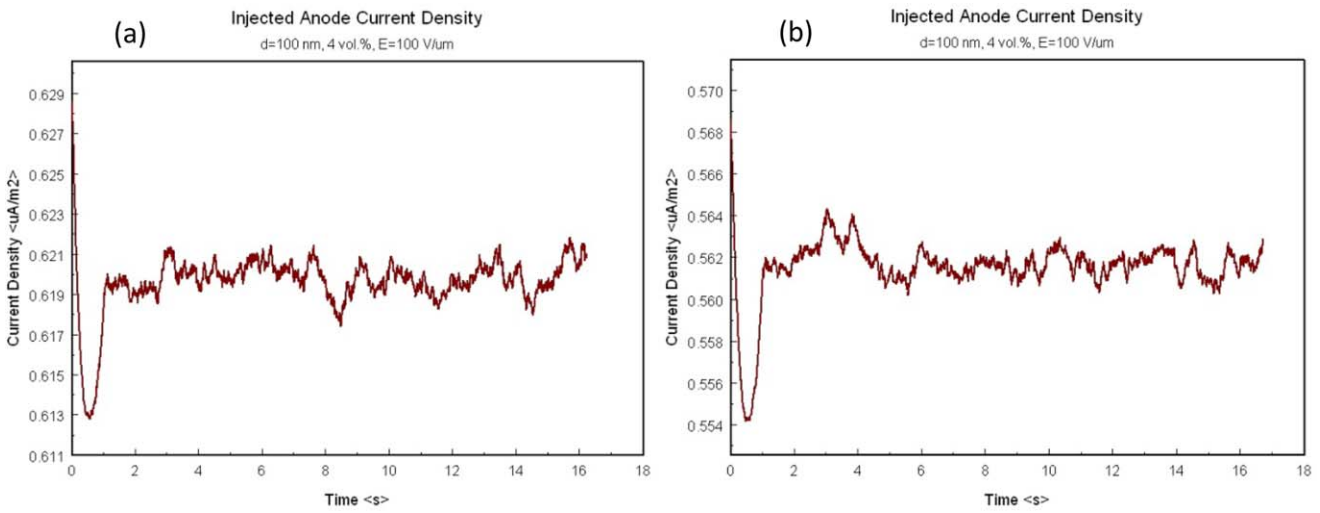

Figure 6. Positive current densities for: (a) dielectric; and (b) conducting nanofillers with initial dips are due to accumulation of injected charge adjacent to the electrodes before arrival of counter charge after 1 transit time. [Color figure can be viewed in the online issue, which is available at wileyonlinelibrary.com.]

nanofillers. The higher conductivity of conducting nanofillers over the dielectric counterpart is probably due to the effect of lower attached net charge where surface migration and ensuing neutralization act to negate the cumulative effect of charging. The trends in leakage conduction are to increase with filler size, and bias $\boldsymbol{E}$ field, and decrease with loading, with the dielectric filler undergoing more rapid changes.

The next set of results examines the trend over the range of filler permittivities which are 5x, 10x, 20x, and 100x the permittivity of the PA/PAI binder; i.e. $\varepsilon_f = 5\varepsilon_b$, $10\varepsilon_b$, $20\varepsilon_b$, and $100\varepsilon_b$. Figure 9(a) shows the calculated effective permittivities up to 66 vol % filler loading. In each case, the effective permittivity value at 100 vol % loading would be that of the filler. Asymptotic limits on the rate of change of effective permittivity with loading in (18) show much higher value when volume fraction $\phi_f \rightarrow 1$ than when $\phi_f \rightarrow 0$, thus explaining the lower values below 50 vol %. Figure 9(b) shows the fractional energies stored in the filler and binder for the four filler permittivities versus loading where it is evident that at higher permittivities most of the energy is stored in the binder due to the vanishingly small filler field.

In Figure 10(a,d) are shown the computed effective permittivities compared against the Weiner lower and upper bounds and the Lichtenecker, Bruggeman, and Maxwell-Garnett rules for the range of filler permittivities. Spline fits are used to span the region between 66 vol.% and 100 vol.%, where each curve is seen to conform quite well in passing through every data point. Several notable features are apparent, and include: (1) The Wiener upper bound for the Lichtenecker rule is the linear interpolation between the filler and binder permittivities, and is identical to the volume fraction approach in (5); (2) Effective permittivities from the PIC energy conserving schemes and the

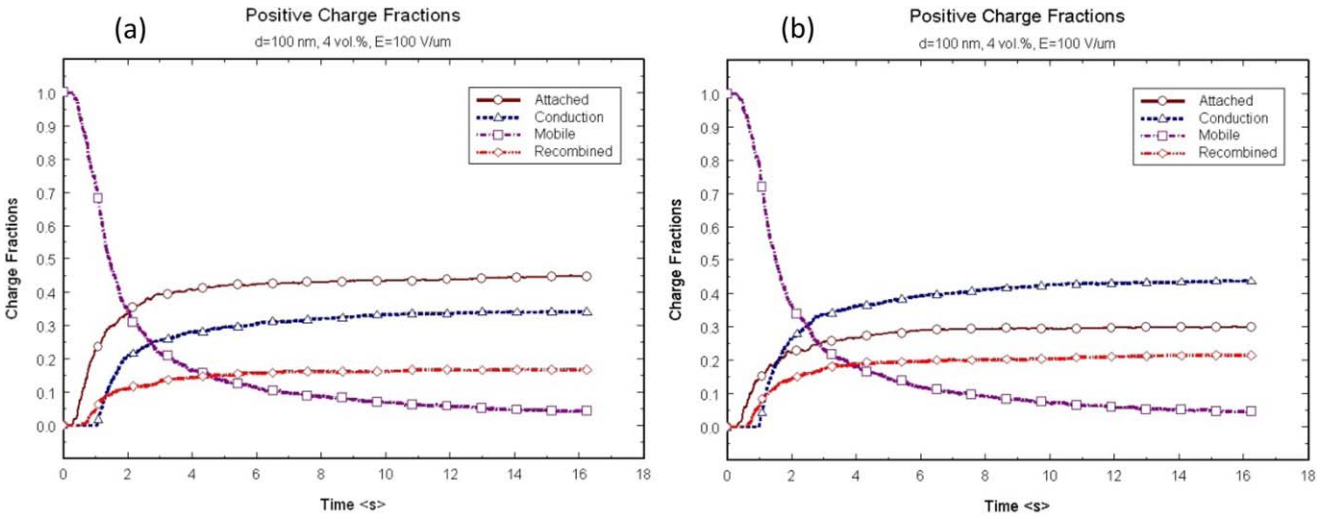

Figure 7. Attached, conduction, mobile, and recombined charge fractions for: (a) dielectric; and (b) conducting nanofillers. [Color figure can be viewed in the online issue, which is available at wileyonlinelibrary.com.]

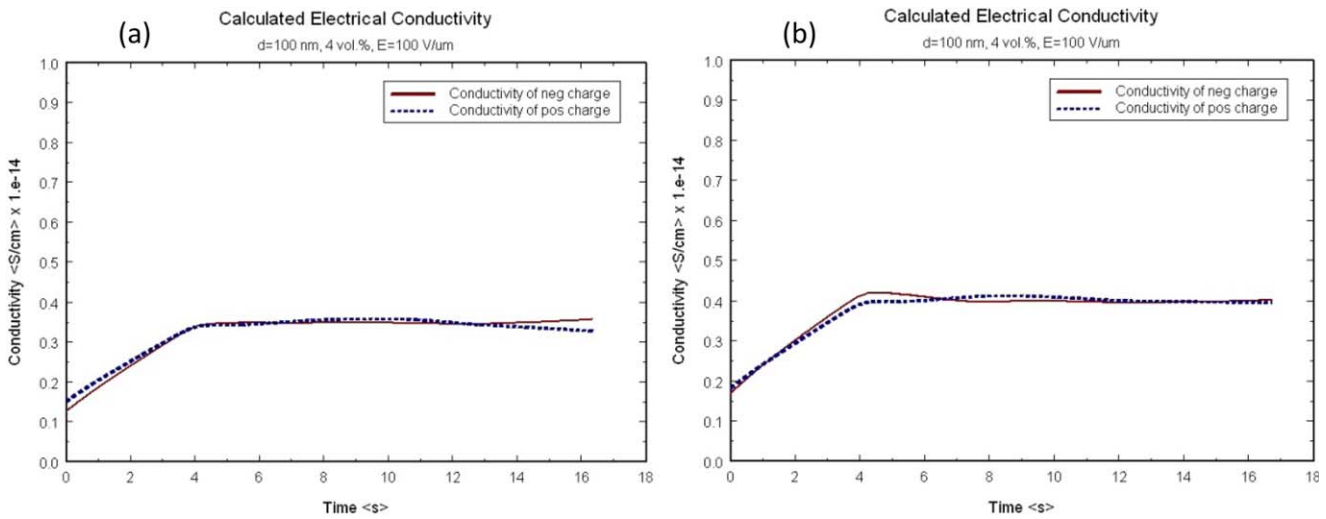

Figure 8. Computed conductivities for 100 nm, 4.0 vol.% loading, and **E**=100 V/μm with bipolar charge injection for: (a) dielectric; and (b) conducting nanofillers. [Color figure can be viewed in the online issue, which is available at wileyonlinelibrary.com.]

Lichtenecker logarithmic rule all lie between the Wiener lower and upper bounds; (3) The Bruggeman rule predicts consistently higher values, beyond 15-20 vol %, due to the assumptions of small permittivity contrast and small Clausius-Mossotti factor; (4) The Maxwell-Garnett rule assumes small volume fractions in addition to the other assumptions for the Bruggeman rule, accounting for the big disparity with the rest at high volume fractions, large permittivity contrast, and small Clausius-Mossotti factor; (5) The Lichtenecker rule, derived directly from the Maxwell-equations, is a fundamental rule with more accurate predictions than either the Bruggeman or Maxwell-Garnett rules; (6) The PIC energy conserving scheme includes the effect of charge transport and resulting field modification (enhancement), and predicts lower values than the Lichtenecker rule given the higher E_{ave} and linear interpolation of the **E** field from (14); (7) The version of the PIC energy conserving scheme using Maxwell-Garnett interpolated **E** field, results in higher values, closer to the Lichtenecker rule, over the entire loading range; (8) At high permittivity contrasts, both PIC energy conserving schemes converge on the Lichtenecker rule at high loading, indicating more accurate predictions; and (9) The predicted permittivities from the Maxwell-Garnett rule and the PIC energy conserving scheme with Maxwell-Garnett **E** field interpolation are nearly coincident and only diverges beyond 60 vol.%, probably due to the charge dynamics and resulting field modification which is not considered by the Maxwell-Garnett rule.

Figure 11(a) shows the interpolation of the **E** field, and the resulting computed effective permittivity using the PIC energy conserving scheme is shown in Figure 11(b). Using the volume fraction approach in (12), akin to linear interpolated **E** field, results in a more conservative lower bound prediction of the effective permittivity. The Maxwell-Garnett interpolation in (16) obtained by substituting **E** for ε results in a higher effective

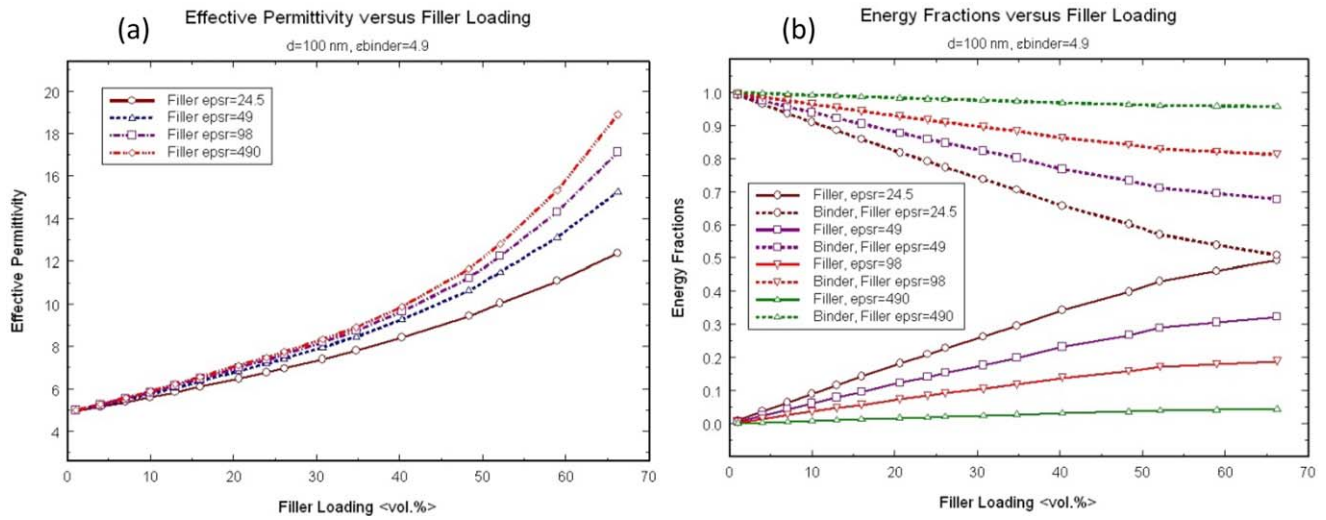

Figure 9. (a) Computed effective permittivities using the PIC energy conserving scheme for ε_f=5ε_b, 10ε_b, 20ε_b, and 100ε_b; and (b) corresponding energy fractions stored in the filler and binder. [Color figure can be viewed in the online issue, which is available at wileyonlinelibrary.com.]

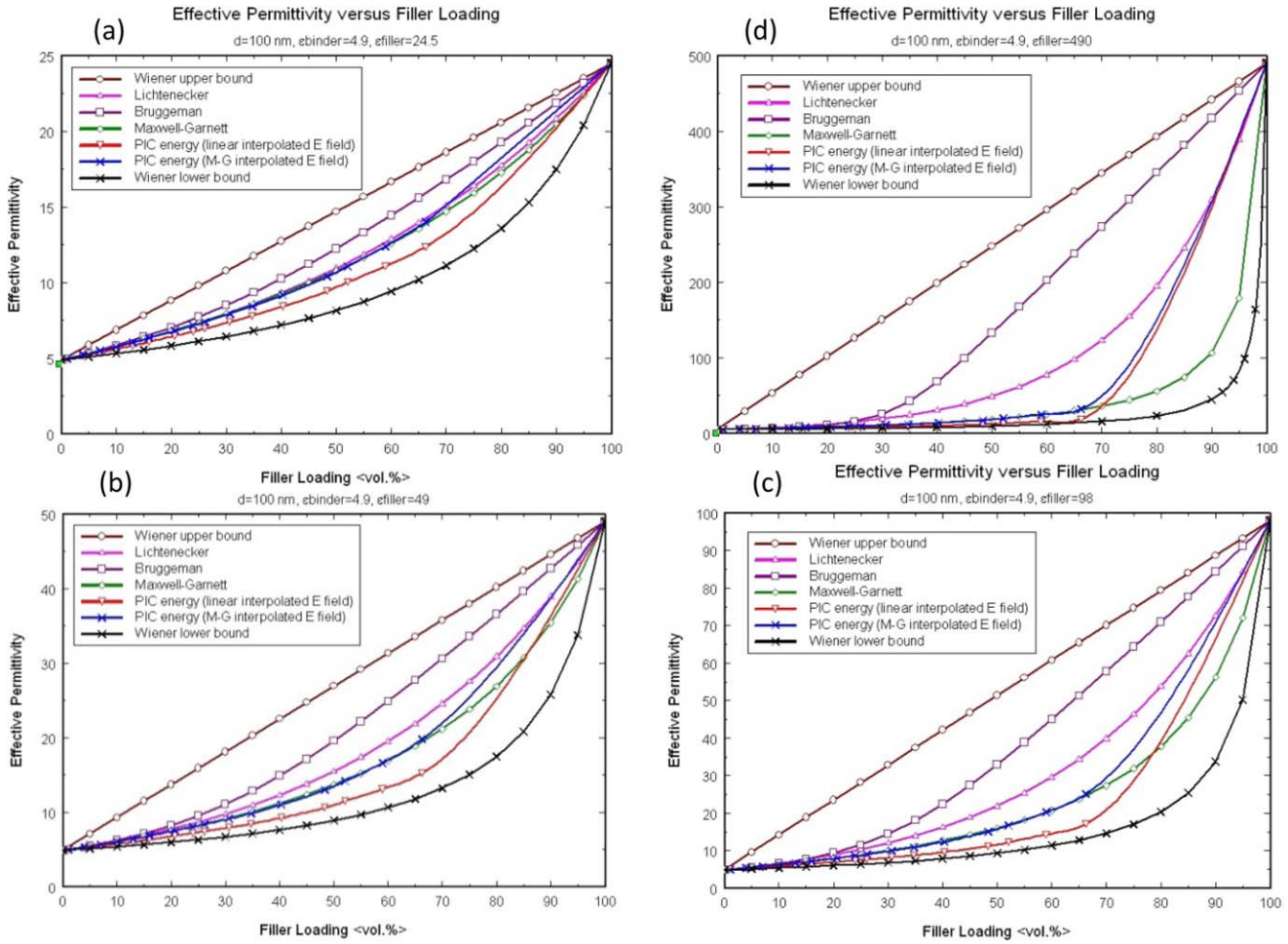

Figure 10. Computed effective permittivity using the PIC energy conserving scheme compared to Wiener bounds and Lichtenecker, Bruggeman, and Maxwell-Garnett rules with $\varepsilon_b=4.9$ over the range of filler loading for: (a) $\varepsilon_f=5\varepsilon_b$; (b) $\varepsilon_f=10\varepsilon_b$; (c) $\varepsilon_f=20\varepsilon_b$; and (d) $\varepsilon_f=100\varepsilon_b$. [Color figure can be viewed in the online issue, which is available at wileyonlinelibrary.com.]

permittivity and may be a better scheme. Conducting fillers result in higher effective permittivity as shown in Figure 12(a), plotted with the family of curves for $\varepsilon_f=5\varepsilon_b$. Figure 12(b) shows comparison of effective permittivities with $\varepsilon_f=10\varepsilon_b$ using both linear and Maxwell-Garnett interpolated **E** fields. The effective permittivity with the conducting filler is much higher than for

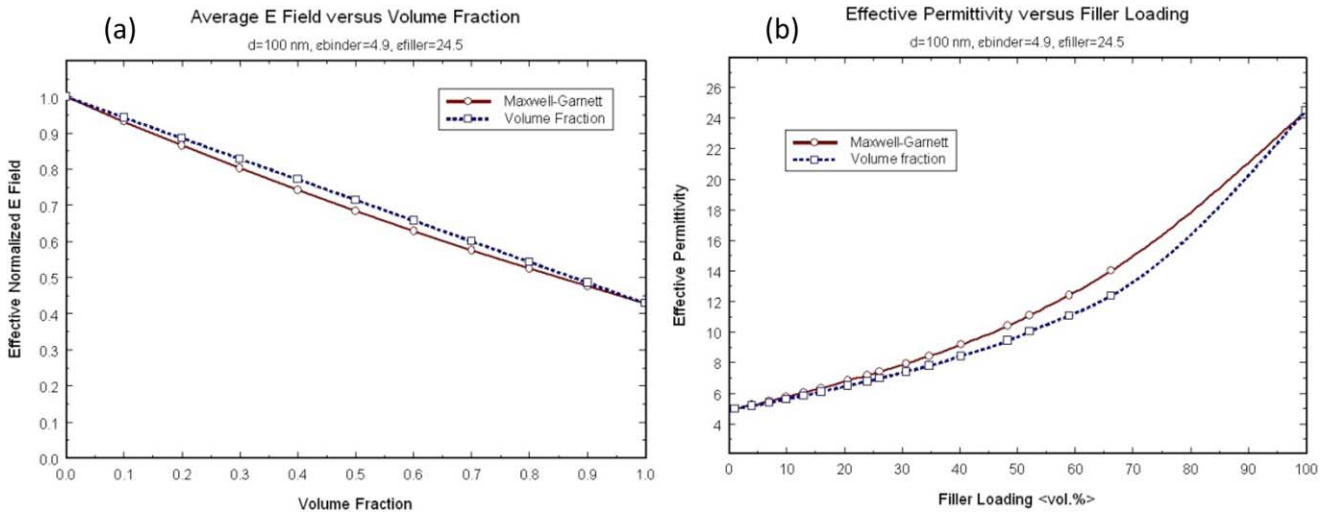

Figure 11. (a) E field interpolation; and (b) resulting computed effective permittivities versus loading using the PIC energy conserving scheme. [Color figure can be viewed in the online issue, which is available at wileyonlinelibrary.com.]

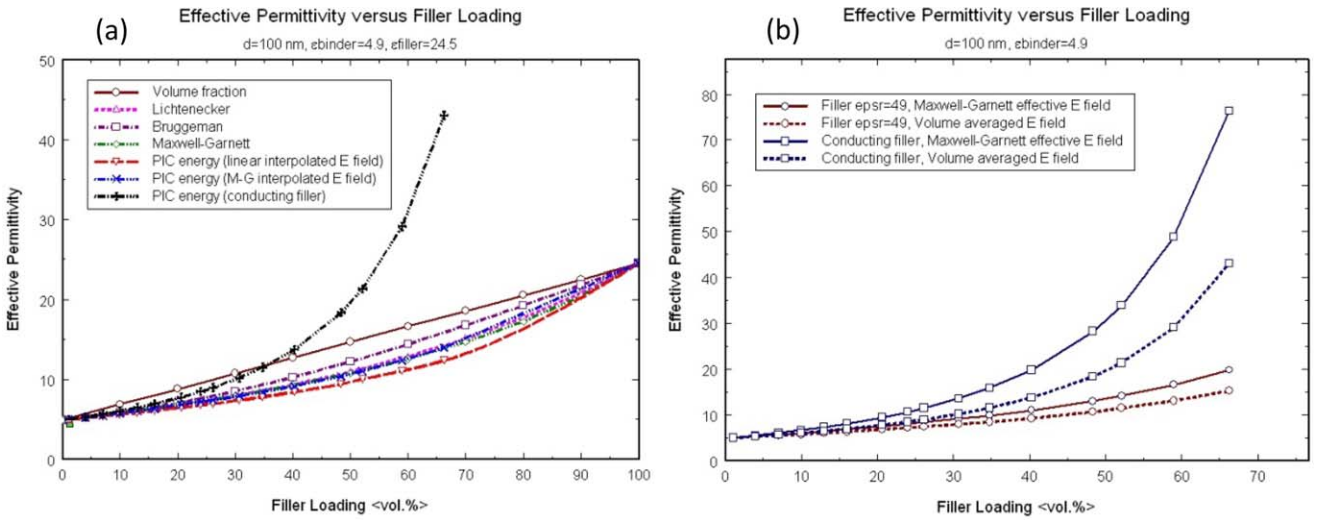

Figure 12. Computed effective permittivity versus loading: (a) with $\varepsilon_f=5\varepsilon_b$ compared to conducting filler; and (b) with $\varepsilon_f=10\varepsilon_b$ compared to conducting fillers and linear and Maxwell-Garnett interpolated **E** fields used in the PIC energy conserving scheme. [Color figure can be viewed in the online issue, which is available at wileyonlinelibrary.com.]

the dielectric filler; agreeing with observations of significant permittivity enhancement.

Shown in Figure 13(a) is the normalized energy density stored in the binder for conducting fillers which peaks at about 25 vol % loading due to the behavior of the $\varepsilon_{eff}E_{ave}^2$ term which has a maxima because ε_{eff} increases while average E_{ave} decreases with increasing loading. The peak is due to the competing effects of higher energy with increasing average field and lower energy with decreasing binder volume. It is clear that this peak will shift with nanofiller size, making it a tunable design criterion. Figure 13(b) compares the stored energy versus filler loading computed from static (Laplacian) and charge transport solutions showing the higher energy of the latter which may be attributed to charge interactions and the resultant field modification. The energy decreases in monotonic manner as the loading increases due to decreasing storage volume of the binder. Finally, the corresponding calculations for dielectric fillers is shown in Figure 14(a) where the stored energy increases at a similar rate to the effective permittivity curve with filler loading for $\varepsilon_f=10\varepsilon_b$. E_{ave} decreases with filler loading in Figure 14(b) as the contribution from the lower **E** field in the filler increases with volume fraction.

CONCLUSIONS

This paper has described the use of a rapid 3D particle simulation algorithm for charge transport through the nanocomposite film comprised of dielectric and conducting nanofillers in

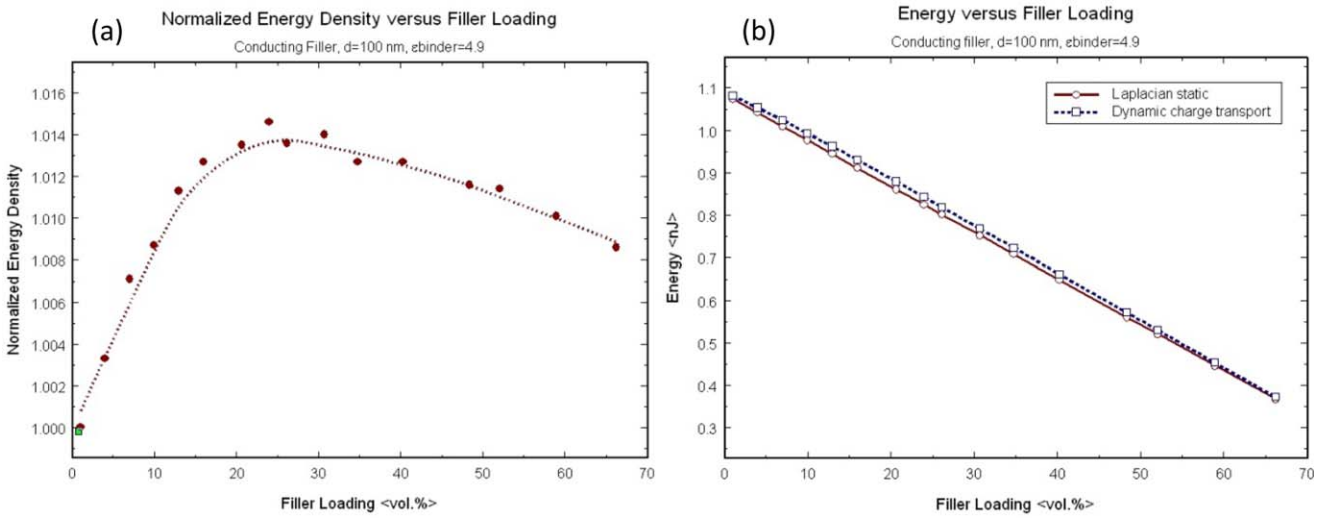

Figure 13. Stored energy (normalized to value at 1 vol.%) as function of loading for conducting filler with $\varepsilon_b=4.9$: (a) showing peak at about 25 vol.% due to contrasting effects of higher field and decreasing binder volume; and (b) comparing static and dynamic calculations where the **E** field is enhanced by trapped and mobile charge. [Color figure can be viewed in the online issue, which is available at wileyonlinelibrary.com.]

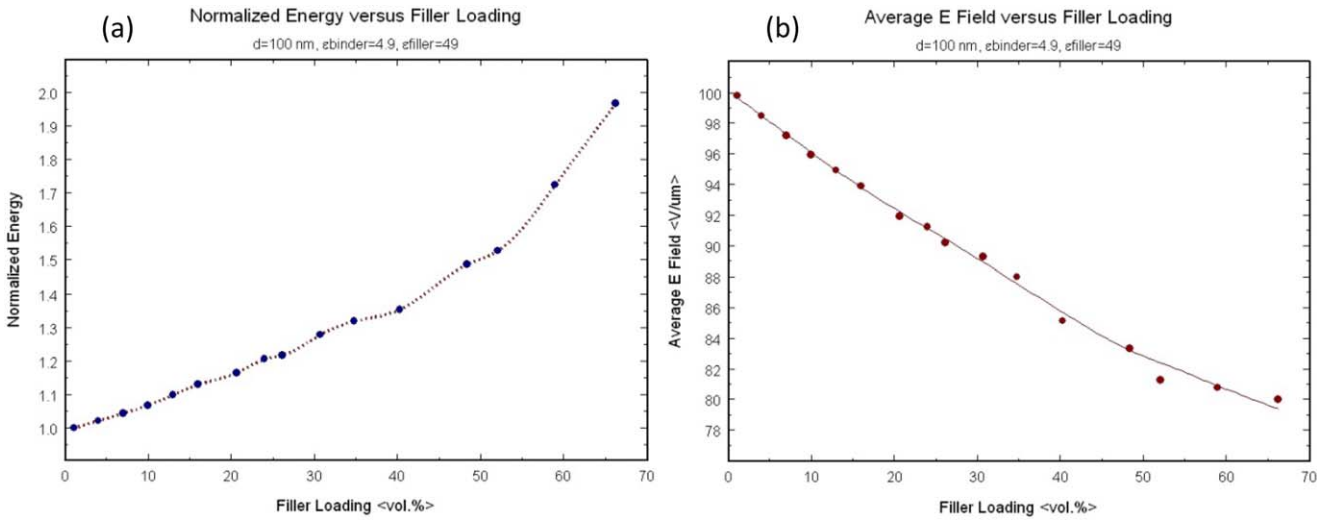

Figure 14. (a) Stored energy (normalized to value at 1 vol.%) as function of loading for dielectric filler with $\varepsilon_f=10\varepsilon_b$, $\varepsilon_b=4.9$; and (b) corresponding E_{ave} which decreases due to increasing filler contribution with lower **E** field. [Color figure can be viewed in the online issue, which is available at wileyonlinelibrary.com.]

amorphous polymer binder to compute stored energy and to derive effective permittivity using an energy conserving scheme.

Simulation results for charge fractions versus loading show differences in behavior with implications to energy storage. Dielectric nanofillers serve the role as trapping sites to prevent charge propagation and eventual accumulation to form packet charge that contribute to failure. Conducting nanofillers at loadings below the percolation threshold are shown to increase the effective permittivity of the nanocomposite film to raise the energy density, confirming accepted conventional understanding.

Effective permittivities computed using the new energy conserving scheme are shown to have excellent agreement with established Lichtenecker, Bruggeman, and Maxwell-Garnett rules especially at low loadings, low contrast, and small Clausius-Mossotti factors. The PIC energy conserving scheme using linear interpolated (volume fraction) ***E*** field results in a lower bound for effective permittivity. The Maxwell-Garnett interpolated ***E*** field improves on the computed effective permittivity, especially at lower volume fractions when it overlays the Maxwell-Garnett mixing rule, indicating the self-consistent behavior of the effective permittivity and interpolated ***E*** field. At higher loading, the two curves diverge showing the difference in neglecting higher order interactions and use of the static ***E*** field solution for the mixing rule. The asymptotic permittivity values at high loading follows the more fundamental Lichtenecker rule. Overall, the energy conserving scheme with Maxwell-Garnett ***E*** field interpolation combines the best of the Maxwell-Garnett and more fundamental Lichtenecker rules and results in the broadest validity over the entire volume fraction range.

The use of dielectric fillers show a monotonic increasing stored energy with increasing loading which also scales with the permittivity contrast. Stored energy with conducting fillers scale linearly with the binder permittivity and exhibits a peak at about 25 vol.% due to the competing effects of higher energy with increasing average field and lower energy with decreasing binder volume. The comparison of stored energy from Laplacian static and dynamic charge transport calculations show that the energy is higher in the latter due to **E** field modification (enhancement) by trapped and mobile charge.

ACKNOWLEDGMENTS

Support by the Department of the Navy, Office of Naval Research, grant N000141310064, is gratefully acknowledged.

REFERENCES

1. Barber, P.; Balasubramanian, S.; Anguchamy, Y.; Gong, S.; Wibowo, A.; Gao, H.; Ploehn, H. J.; zur Loye, H. C. *Materials* **2009**, *2*, 1697.
2. Wang, Q.; Zhu, L. *J. Polym. Sci. Part B: Poly. Phys.* **2011**, *49*, 1421.
3. Gallot-Lavallee, O.; Griseri, V.; Teyssedre, G.; Laurent, C. *Rige* **2005**, *8*, 749.
4. Sessler, G. M.; West, J. E.; Gerhard, G. *Phys. Rev. Lett.* **1982**, *48*, 560.
5. Boukhris, I.; Belgaroui, E.; Kallel, A. *Int. J. Elec. Eng. Inform.* **2010**, *2*, 313.
6. Chen, G.; Loi, S. H. *Proc. Mat. Res. Soc. Fall Meeting* **2006**, Boston.
7. Lean, M. H.; Chu, W.-P. L. *IEEE Trans. Diel. Elec. Ins.* **2014**, *21*, 1319.
8. Lean, M. H.; Chu, W.-P. L. *J. Phys. D: Appl. Phys.* **2014**, *47*, 075303.
9. Lean, M. H.; Chu, W.-P. L. *COMPEL: Int. J. Comp. Math. Elec. Elec. Eng.* **2014**, *33*, 1396.

10. Pisa, D.; Danikas, M. G. *NANO: Brief Rep. Rev.* **2011**, *6*, 497.
11. Goncharenko, A. V.; Lozovski, V. Z.; Venger, E. F. *Opt. Comm.* **2000**, *174*, 19.
12. Karkkainen, K. K.; Sihvola, A. H.; Nikoskinen, K. I. *IEEE Trans. Geosci. Remote Sensing* **2000**, *38*, 1303.
13. Stroud, D. *Superlattices Microstruct.* **1998**, *23*, 567.
14. Chang, H.-M.; Liao, C. *World J. Cond. Mat. Phys.* **2011**, *1*, 55.
15. Simkin, R. A. *IEEE Trans. MTT* **2010**, *58*, 545.
16. Mekala, R.; Badi, N. *Proc. 2013 COMSOL Conference* **2013**, Boston.
17. Koledintseva, M. Y.; Patil, S. K.; Schwartz, R. W.; Huebner, W.; Rozanov, K. N.; Shen, J.; Chen, J. *IEEE Trans. DEI* **2009**, *16*, 793.
18. Patil, S. K.; Koledintseva, M. Y.; Schwartz, R. W.; Huebner, W. *J. Appl. Phys.* **2008**, *104*, 074108.
19. Lean, M. H.; Chu, W.-P. L. *J. Appl. Phys.* **2015**, *117*, 104102.
20. Lean, M. H.; Chu, W.-P. L. *J. Polym.* **2015**, *2015*, 1.
21. Lean, M. H.; Chu, W.-P. L. *Special Issue IEEE Trans. Diel. Elec. Ins. Electrets Related Phenomena* **2015**, *22*, 1444.
22. Lean, M. H.; Chu, W.-P. L. *J. Polym. Sci. Part B: Polym. Phys.* **2015**, *53*, 1380.
23. Gottlieb, S.; Shu, C. W.; Tadmor, E. *SIAM Rev.* **2001**, *43*, 89.
24. Hockney, R. W.; Eastwood, J. W. In Computer Simulation Using Particles; McGraw-Hill: New York, **1981**.
25. Dawson, J. M. *Rev. Mod. Phys.* **1983**, *55*, 403.
26. Birdsall, C. K. *IEEE Trans. Plasma Sci.* **1991**, *19*, 65.
27. Caughey, D. M.; Thomas, R. E. *Proc. IEEE* **1967**, *55*, 2192.
28. Abramowitz, A.; Stegun, I. A. In Handbook of Mathematical Functions; Dover Press: New York, **1965**; p 591.
29. Le Roy, S.; Teyssedre, G.; Laurent, C. *IEEE Trans. Diel. Elec. Ins.* **2005**, *12*, 644.